This is the accepted manuscript made available via CHORUS. The article has been published as:

Incommensurate Magnetism Near Quantum Criticality in CeNiAsO

Shan Wu, W. A. Phelan, L. Liu, J. R. Morey, J. A. Tutmaher, J. C. Neuefeind, Ashfia Huq, Matthew B. Stone, M. Feygenson, David W. Tam, Benjamin A. Frandsen, Benjamin Trump, Cheng Wan, S. R. Dunsiger, T. M. McQueen, Y. J. Uemura, and C. L. Broholm

Phys. Rev. Lett. **122**, 197203 — Published 15 May 2019

DOI: 10.1103/PhysRevLett.122.197203

Incommensurate magnetism near quantum criticality in CeNiAsO

Shan Wu,[1,2,*] W. A. Phelan,[1] L. Liu,[3] J. R. Morey,[1] J. A. Tutmaher,[1] J. C. Neuefeind,[4] Ashfia Huq,[5] Matthew B. Stone,[5] M. Feygenson,[6] David W. Tam,[7] Benjamin A. Frandsen,[8] Benjamin Trump,[9] Cheng Wan,[1] S. R. Dunsiger,[10] T. M. McQueen,[1,11] Y. J. Uemura,[3] and C. L. Broholm[1,11,12]

[1]*Department of Physics and Astronomy and Institute for Quantum Matter, Johns Hopkins University, Baltimore, Maryland 21218, USA*
[2]*Department of Physics, University of California Berkeley, Berkeley, California 94720, USA*
[3]*Department of Physics, Columbia University, New York, New York 10027, USA*
[4]*Oak Ridge National Laboratory, Chemical and Engineering Materials Division, Oak Ridge, Tennessee 37831, USA*
[5]*Oak Ridge National Laboratory, Neutron Scattering Division, Oak Ridge, Tennessee 37831, USA*
[6]*Juelich Centre for Neutron Science, Forschungszentrum Juelich GmbH, 52425 Juelich, Germany*
[7]*Department of Physics and Astronomy, Rice University, Houston, Texas 77005, USA*
[8]*Department of Physics, Brigham Young University, Provo, Utah 84602, USA*
[9]*NIST Center for Neutron Research, National Institute of Standards and Technology, Gaithersburg, Maryland 20899, USA*
[10]*Department of Physics, Simon Fraser University, Burnaby, B.C., Canada*
[11]*Department of Materials Science and Engineering, Johns Hopkins University, Baltimore, Maryland 21218, USA*
[12]*Oak Ridge National Laboratory, Quantum Condensed Matter Division, Oak Ridge, Tennessee 37831, USA*

(Dated: March 28, 2019)

We report the discovery of incommensurate magnetism near quantum criticality in CeNiAsO through neutron scattering and zero field muon spin rotation. For $T < T_{N1} = 8.7(3)$ K, a second order phase transition yields an incommensurate spin density wave with wave vector $\mathbf{k} = (0.44(4), 0, 0)$. For $T < T_{N2} = 7.6(3)$ K, we find co-planar commensurate order with a moment of 0.37(5) μ_B, reduced to 30 % of the saturation moment of the $|\pm\frac{1}{2}\rangle$ Kramers doublet ground state, which we establish through inelastic neutron scattering. Muon spin rotation in $\mathrm{CeNiAs_{1-x}P_xO}$ shows the commensurate order only exists for x $\leq$ 0.1 so we infer the transition at $x_c = 0.4(1)$ is between an incommensurate longitudinal spin density wave and a paramagnetic Fermi liquid.

The competing effects of intra-site Kondo screening and inter-site Ruderman-Kittel-Kasuya-Yosida (RKKY) interactions in rare earth intermetallics epitomize the strongly correlated electron problem. While the Néel and Kondo lattice limits are well understood [1], the transition between them is far from. It involves an increase in the volume enclosed by the Fermi surface (FS) as the $4f$ electron is incorporated on the Kondo lattice side of the transition[2, 3]. Deviations from the $\rho \propto T^2$ dependence of resistivity is interpreted as indicative of the associated quantum criticality, which is denoted as "local" because it involves the entire FS. In support of this concept, compounds with the requisite transport anomalies have been discovered where physical properties that involve averages over distinct regions of momentum space have related critical exponents. The eventual transition to magnetic order when RKKY interactions dominate can coincide with the localization transition or occur within the large or small FS phases. Clearly the nature of the corresponding quantum critical point is strongly affected as magnetic ordering is momentum selective and breaks time reversal symmetry.

Exploration of model systems is essential to uncover the overall phase diagram of this complex strongly correlated regime. $\mathrm{CeCu_{6-x}Au_x}$ provided a first example of local criticality. de Haas-van Alpen measurements provide evidence for an abrupt rearrangement of the FS in $\mathrm{CeRhIn_5}$ at 2.25 GPa [4–6] . A step change in the Hall coefficient of $\mathrm{YbRh_2Si_2}$ coupled with anomalous and yet unexplained critical exponents at the field driven ferromagnetic transition have been interpreted as evidence the magnetic and the electron localization transitions coincide[7–11]. Each compound adds unique insights and distinct experimental opportunities.

Isostructural to the 1111 iron pnictides, CeNiAsO is an exciting new addition to the landscape of strongly correlated electron systems [12]. Magnetically ordered at low$-T$ and ambient pressure, substitution of P for As or pressure drives $\mathrm{CeNiAs_{1-x}P_xO}$ to a paramagnetic Fermi-liquid. Non-Fermi-liquid transport is found up to the critical pressure $P_c = 6.5$ kbar and the critical composition $x_c = 0.4(1)$ and a sign change in the Hall coefficient at P_c indicates FS reconstruction [13]. CeNiAsO differs from other systems studied to date in having two magnetic phase transitions [12].

In this letter we determine the corresponding magnetic phases and examine their interplay with FS reconstruction. We show the upper transition is to an incommensurate longitudinal SDW state with wave vector $\mathbf{k} = (0.44(4), 0, 0)$ that closely matches the umklapp wave vector $(2\mathbf{k}_f)$ of the small FS. The second transition yields co-planar commensurate order with a low$-T$ ordered moment reduced to 30% of the saturation moment of the nominal $|\pm\frac{1}{2}\rangle$ Kramers doublet ground state. P doping suppresses the commensurate phase but retains the SDW perhaps all the way to the critical

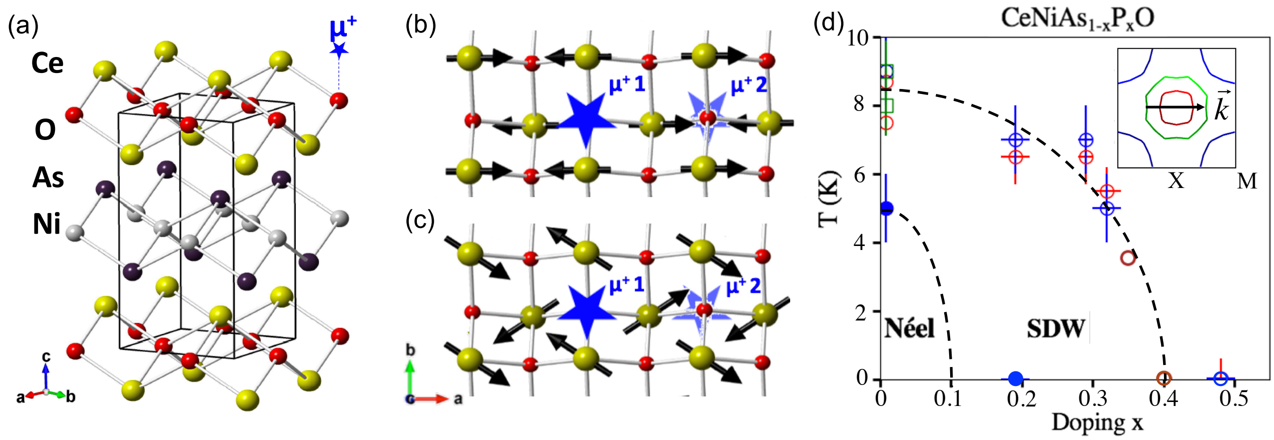

FIG. 1: (a) Crystallographic structure of CeNiAsO, and spin structure for $T_{N2} < T < T_{N1}$ (b) and $T < T_{N2}$ (c). Blue stars indicate the single crystallographic muon site. Two equivalent muon sites above and below oxygen site become inequivalent within the magnetically ordered state. (d) Temperature-doping phase diagram. Red, blue, and green symbols are from specific heat, μSR, and neutron data respectively. Brown dots are from Luo et al. [13]. We assign open (closed) symbols to the higher (lower) T transition. The inset to (d) shows the $q_z = 0$ small Fermi surface excluding $4f$ electrons. The arrow shows the magnetic wave vector, which connects extended areas of the Fermi surface. The dashed lines are guides to the eye.

concentration where the FS grows to include $4f$ electrons.

We probed the magnetism of CeNiAsO through magnetic neutron scattering on the NOMAD and POWGEN diffractometers [14, 15] and on the SEQUOIA [16] spectrometer at the Spallation Neutron Source. For complementary real space information we used muon spin rotation (μSR) at the M15 beam line at TRIUMF. Specific heat measurements were conducted on a 14 Tesla Quantum Design PPMS with a dilution fridge insert.

Fig. 1(a) shows the tetragonal structure of CeNiAsO where magnetism is associated with Ce^{3+} sandwiching a square lattice of oxygen. The structure and the single phase nature of the sample was ascertained by Rietveld refinement of high resolution neutron diffraction data (see SI). The specific heat data in Fig. 3(d) show shoulder-like anomalies indicating two second order phase transitions at $T_{N1} = 9.0(3)$ K and $T_{N2} = 7.6(3)$ K. The inferred critical temperatures are consistent with previously published specific heat data with sharper peaks indicating higher purity[12]. The rounded maxima shift towards lower T and approach each other in a field of $\mu_0 H = 14$ T as for two distinct antiferromagnetic phases.

To determine their nature, we use zero field μSR in the longitudinal configuration [17, 18]. Fig. 2 shows muon spin precession indicative of a well defined static internal field for $T < T_{N1}$. A qualitative change in the μSR profile for $T < T_{N2}$ indicates two distinct magnetic phases. For $T_{N2} < T < T_{N1}$, muons sample the broad spectrum of local fields generated by an incommensurate SDW [19]. For $T < 6$ K, the signal is oscillatory (Fig. 2 (b)) with a beating pattern that indicates two distinct precession frequencies and commensurate magnetism. These patterns can be fitted by magnetic structures that are consistent with the neutron data and a single crystallographic muon stopping site.

We determined the fundamental magnetic wave vector and spin polarization through neutron diffraction. Weak magnetic peaks are apparent at $T = 2$ and 8 K after subtracting data at $T = 15$ K (Fig. 2 (c-d)). At $T = 2$ K, the difference pattern shows several resolution limited peaks. The peak with the lowest wave vector transfer $Q \approx 0.77$ Å^{-1} can be indexed as $\mathbf{Q}_m = (0.5, 0, 0)$. Magnetic neutron diffraction probes spin polarization perpendicular to wave vector transfer so this indexing implies spin components along $\mathbf{b}$ and/or $\mathbf{c}$. Upon warming to 8 K $< T_{N1}$, the absence of this first peak is indicative of a longitudinal spin density wave (SDW) polarized along $\mathbf{a}$. The width of the intensity maxima for $T = 8$ K and $Q \approx 1.1$ Å^{-1} in Fig. 2 (c) exceeds the instrumental Q-resolutions. The incommensurability indicated by μSR can account for this. The magnetic signal at 8 K is however quite weak and since there is no energy resolution, inelastic magnetic scattering may also contribute to the broadened peaks, particularly near the polarization suppressed $\mathbf{Q}_m$ peak. The diffraction data thus do not permit a unique determination of the spin structure for $T_{N2} < T < T_{N1}$.The combination of muon, specific heat, and elastic/inelastic neutron data, however, does allow an accurate determination of both structures.

Using Kovalev notation [20, 21], the reducible magnetic representation associated with $\mathbf{k} = (\mu 00)$ decomposes into three two-dimensional irreducible representations (IR): $\Gamma_{mag} = 2\Gamma_1^{(2)} + \Gamma_2^{(2)}$ with 6 Basis Vectors (BVs) (Table S2). Landau theory allows only one IR for each of the two second order phase transitions. Below T_{N1}, BVs $\psi(4)$ and $\psi(6)$ of Γ_1 depict a spin structure with

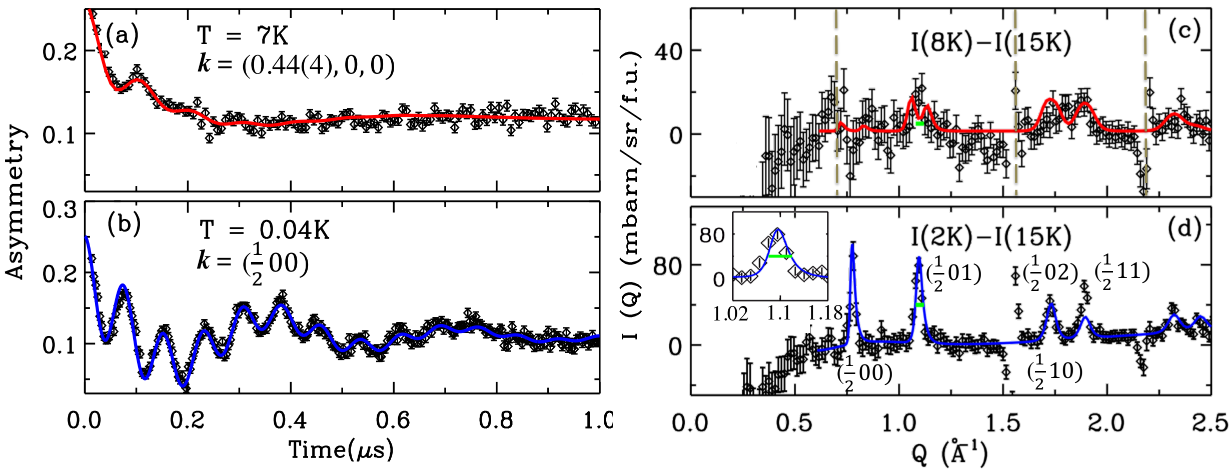

FIG. 2: (a-b) Zero-field longitudinal configuration μSR spectra at $T = 7$ K and 0.05 K. The colored lines were calculated for the magnetic structures of Fig. 1. (c-d) Diffraction patterns collected at $T = 2$ K and 8 K on NOMAD, after subtracting T = 15 K data as a measure of nuclear diffraction. Red and blue lines correspond to the spin configurations in Fig. 1. The grey dashed lines in (c) mark the nuclear Bragg positions, where thermal expansions gives rise to a peak-derivative anomaly. In (d) the horizontal green bar at $Q = 1.1\text{Å}^{-1}$ indicates the instrument resolution of 0.04 Å^{-1} as detailed in the inset.

moments along **a**. Adding $\psi(3)$ and $\psi(5)$ allows for moments along **c**. Below T_{N2}, we can account for the diffraction pattern in Fig. 2 (d) by adding $\psi(1)$ and $\psi(2)$ of Γ_2. The best fit corresponds to a reduced $\chi^2 = 1.95$ and a staggered moment $\langle m \rangle = 0.37(5)$ μ_B/Ce that is canted by $\varphi \approx 36(6)^\circ$ to the **a** axis (Fig. 1 (c)). While allowed by symmetry, the diffraction data place a limit of 0.06 μ_B on any **c**-component of the staggered moment.

μSR, which probes magnetism in real space, offers an independent assessment of the proposed structures. We find a consistent description of the precession data with the muon stopping site $(\frac{1}{4}, \frac{3}{4}, z_\mu)$ in Fig.1 (a). The fitting analysis described below yields $z_\mu = 0.1471(3)$ ($=z_{\text{Ce}}$), close to the preferred distance of muons from O^{2-} [22]. This location is also favored considering the electrostatic potential-energy map for CeFeAsO [23]. The observation of two muon precession frequencies suggests two magnetically inequivalent muon sites (see Fig.1 (b-c)). The asymmetry pattern $P_\mu^z(t)$ can be fitted to equation S1 wherein the magnetic field distribution function $\rho_i(B)$ is calculated directly from the spin structures. For the low T commensurate state, $\rho_i(B)$ consists of two delta functions corresponding to the magnetic field at each of the two magnetically inequivalent (but crystallographically equivalent) muon sites. The best fit is obtained with moment $m = 0.37(2)\mu_B$ and rotation angle $\varphi = 36(7)^\circ$, which is in excellent agreement with the Rietveld refinement of neutron diffraction. For the high T incommensurate state, $\rho_i(B)$ is continuous: The incommensurate nature of the spin structure ensures every muon site, though crystallographically equivalent, is magnetically unique and contributes a distinct precession frequency. The best fit leads to an incommensurate wave vector **k**=(0.44(4),0,0), $m_a = 0.27(6)\mu_B$, and $m_c = 0.08(3)\mu_B$. The corresponding calculated muon asymmetry and neutron diffraction are in Fig. 2 (a)&(c). A small component of m_c implies this is a magnetic cycloid. The corresponding lack of inversion symmetry could have interesting consequences for electronic transport. However, since $m_c \ll m_a$ we retain the terminology of a longitudinal SDW. In summary, the spin structures for two ordered states – a longitudinal SDW (Fig. 1 (b), Fig. S4) and a commensurate coplanar structure (Fig. 1 (c)) – account for both neutron and μSR data.

For context we examine the $4f$ electron crystal field excitations through inelastic magnetic neutron scattering (Fig. 4(a-e)). At $T = 7$ K, the intensities of modes at E $\approx$ 10 meV, 30 meV and 40 meV rise with Q^2 and are observed both for CeNiAsO and non-magnetic LaNiAsO and so must be vibrational[27]. In the difference data $\tilde{I}(Q,E)$ and $\tilde{I}(E)$ (Fig. 4 (c-e)), we associate the two broad modes at $E_1 \approx 18(3)$ meV and $E_2 \approx 70(8)$ meV with magnetic excitations because their intensity decreases with Q as the $4f$ formfactor. In the tetragonal environment of Ce^{3+}, the $J = \frac{5}{2}$ multiplet splits into three Kramer's doublets. The two magnetic modes are correspondingly assigned to crystal-field-like excitations from the ground state (GS) to two excited doublets. At $T = 200$ K population of the excited state yields a broad mode at 50 meV$\approx E_2 - E_1$, which arises from excitations between the excited doublets. Finally we observe a sharp mode at $E_0 \approx 2$ meV within the AFM ordered state (inset, Fig.4 (d)). In the language of CEF theory, this is an intra-doublet transition driven to inelasticity by the molecular exchange field. As expected for a strongly correlated solid, the crystal field excitations measured for a powder sample are broadened by damping and

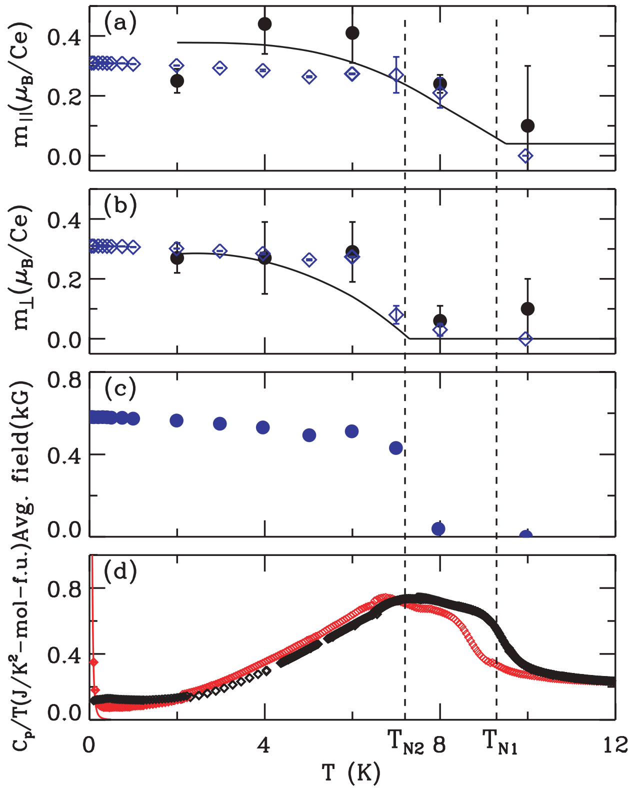

FIG. 3: Temperature dependence of (a) the longitudinal (m_a) and (b) the transverse moments (m_c for high T and m_b for low T phase). Black dots were extracted from Rietveld fits to neutron diffraction data. The 2 K and 8 K data points were averaged over two chopper settings. Blue diamonds were inferred from μSR fits. The solid lines are guides to the eye. (c) Temperature dependence of the averaged static field. (d) Specific heat C_p/T in zero field and for $\mu_0 H = 14$ T. The upturn in C_p/T at 14 T is due to the nuclear spin contributions as indicated by the solid red line.

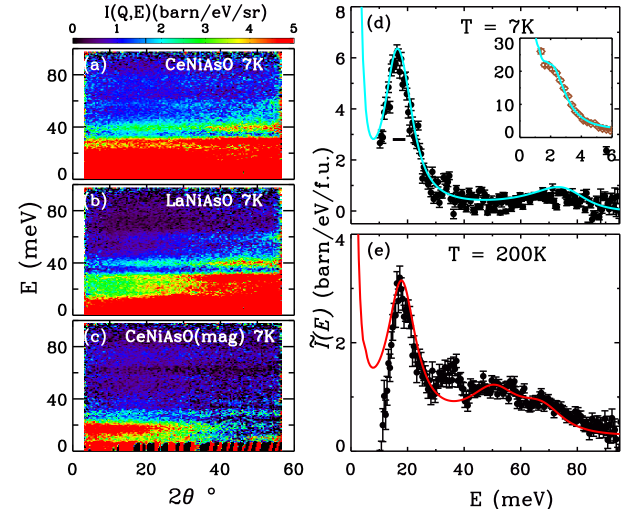

FIG. 4: Normalized inelastic spectrum with incident energy $E_i = 100$ meV (black dots) for (a) CeNiAsO and (b) the non-magnetic reference LaNiAsO. (c) The $T = 7$ K difference spectrum: $\tilde{I}(Q,E) = I_{Ce} - rI_{La}$ where $r = \sigma_{\mathrm{CeNiAsO}}/\sigma_{\mathrm{LaNiAsO}}$. (d-e) Momentum-integrated scattering at $T = 7$ K and 200 K by using the method in Ref. [24–26]. The horizontal black bar indicates energy resolution. The inset in (d) shows a magnetic excitation at 2 meV in the ordered state with $E_i = 50$ meV (brown dots). The cyan and red solid lines were calculated for the crystal field model described in the text.

dispersion, leading to the half width at half maximum (HWHM) of $\Gamma_1 = 13$ meV and $\Gamma_3 = 24$ meV. Fitting to Lorentzian spectral functions leads to HWHM of $\Gamma_0 = 2$ meV that is comparable to the Kondo temperature $T_K = 15(5)$ K inferred from thermo-magnetic data [12].

Given these broad modes, a local moment crystal field model cannot be comprehensive but it provides a useful starting point. As detailed in the SI, we carried out a global fit of a symmetry-constrained crystal field model to the normalized scattering data $\tilde{I}(E)$ at $T = 7$ K and 200 K. After optimizing the crystal field parameters a molecular exchange field and three transition specific relaxation rates, Fig. 4(d-e) shows a consistent description of data from two instrumental configurations and two temperatures is achieved. The model also accounts for the temperature dependent susceptibility data. Consistent with the easy plane (ab plane) character of the ordered states, the GS wave function is $|\pm\frac{1}{2}\rangle$ (Γ_7).

As indicated in the DFT FS plot (Fig. 1 (d)), the ordering wave vector $\mathbf{k} = (0.44(4), 0, 0)$ satisfies a nesting condition. This suggests the ordered state for $T_{N2} < T < T_{N1}$ should be classified as a SDW [28–32]. It is common for incommensurate (IC) magnets to undergo a longitudinal to transverse spin reorientation transition that reduces the modulation in the magnitude of the dipole moment per unit cell while sustaining the IC modulation [30, 33]. The situation is different for CeNiAsO, which not only develops transverse magnetization but also becomes commensurate for $T < T_{N2}$. To arrive at the spin structure in Fig. 1 (c) from the commensurate version of Fig. 1 (b) involves counter-rotating the upper and lower AFM layers of a CeO sandwich (Fig. 1 (a)) by $\varphi = 36°(5)$ around $\mathbf{c}$. While inter-layer bi-linear interactions vanish at the mean field level for $\mathbf{k} = (0.5, 0, 0)$ type order, inter-layer bi-quadratic interactions[34, 35] give rise to a term in the free energy of the form $(m^2 \cos 2\varphi)^2$ that can favor $\varphi = 45^o$ for a commensurate structure only. As m grows upon cooling this term can be expected to induce both the IC to commensurate transition and the symmetry breaking transverse magnetization at T_{N2}.

This brings us to the character of magnetism in $\mathrm{CeNiAs_{1-x}P_xO}$. Upon cooling, CeNiAsO passes from Fermi liquid to IC SDW to commensurate non-collinear order in two second order phase transitions. P doped samples that we examined ($\mathrm{CeNiAs_{1-x}P_xO}$ for $x > 0.1$)

all show the characteristic μSR oscillation associated with IC magnetism (Fig.2 (a)) down to 50 mK. This indicates the commensurate state is limited to a low T, low x pocket (Fig. 1 (d)) and the initial instability of the strongly correlated Fermi liquid in $\mathrm{CeNiAs_{1-x}P_xO}$ is to an IC SDW. An important open question is whether the characteristic wave vector of the SDW evolves with x or continues to be associated with the small FS as for $x = 0$.

We thank Gerald Morris, Bassam Hitti, and Iain McKenzie for μSR beam line support, Sky Cheung and Yipeng Cai for assistance during the μSR experiment, and Allen Scheie for useful discussions on crystal field analysis. This research was funded by the US Department of Energy, office of Basic Energy Sciences, Division of Material Sciences and Engineering under grant DE-SC0019331 and by the Gordon and Betty Moore foundation through GBMF4532. The research at ORNL's Spallation Neutron Source was sponsored by the Scientific User Facilities Division, Office of Basic Energy Sciences, U.S. Department of Energy. Activities at Columbia and TRIUMF were supported by NSF DMR-1436095 (DMREF) and DMR-1610633, and the REIMEI project of Japan Atomic Energy Agency.

* Electronic address: shanwu@berkeley.edu

[1] S. Doniach, Physica B+C **91**, 231 (1977).
[2] P. Gegenwart, Q. Si, and F. Steglich, Nature Phys. **4**, 186 (2008).
[3] P. Coleman and A. J. Schofield, Nature **433**, 226 (2005).
[4] L. Jiao, Y. Chen, Y. Kohama, D. Graf, E. D. Bauer, J. Singleton, J.-X. Zhu, Z. Weng, G. Pang, T. Shang, et al., Proceedings of the National Academy of Sciences **112**, 673 (2015).
[5] T. Park, F. Ronning, H. Q. . Yuan, M. B. Salamon, R. Movshovich, J. L. Sarrao, and J. D. Thompson, Nature **440 7080**, 65 (2006).
[6] H. Shishido, R. Settai, H. Harima, and Y. ?nuki, Journal of the Physical Society of Japan **74**, 1103 (2005).
[7] C. Stock, C. Broholm, F. Demmel, J. Van Duijn, J. W. Taylor, H. J. Kang, R. Hu, and C. Petrovic, Phys. Rev. Lett. **109**, 127201 (2012).
[8] S. Friedemann, T. Westerkamp, M. Brando, N. Oeschler, S. Wirth, P. Gegenwart, C. Krellner, C. Geibel, and F. Steglich, Nature Physics **5**, 465 (2009), ISSN 1745-2473.
[9] S. Paschen, T. Lhmann, S. Wirth, P. Gegenwart, O. Trovarelli, C. Geibel, F. Steglich, P. Coleman, and Q. Si, Nature **432**, 881885 (2004), ISSN 0028-0836.
[10] S. Paschen, T. Lühmann, S. Wirth, P. Gegenwart, O. Trovarelli, C. Geibel, F. Steglich, P. Coleman, and Q. Si, Nature **432**, 881 (2004).
[11] S. Friedemann, N. Oeschler, S. Wirth, C. Krellner, C. Geibel, F. Steglich, S. Paschen, S. Kirchner, and Q. Si, Proc. National Academy of Sciences **107**, 14547 (2010).
[12] Y. Luo, H. Han, H. Tan, X. Lin, Y. Li, S. Jiang, C. Feng, J. Dai, G. Cao, Z. Xu, et al., J. Phys.: Cond. Matter **23**, 175701 (2011).
[13] Y. Luo, L. Pourovskii, S. Rowley, Y. Li, C. Feng, A. Georges, J. Dai, G. Cao, Z. Xu, Q. Si, et al., Nature Mat. **13**, 777 (2014).
[14] J. Neuefeind, M. Feygenson, J. Carruth, R. Hoffmann, and K. K. Chipley, Nuclear Instruments and Methods in Phys. Res. B: Beam Interactions with Materials and Atoms **287**, 68 (2012), ISSN 0168-583X.
[15] A. Huq, J. P. Hodges, O. Gourdon, and L. Heroux, Z. Kristallogr. Proc **1**, 127 (2011).
[16] G. E. Granroth, A. I. Kolesnikov, T. E. Sherline, J. P. Clancy, K. A. Ross, J. P. C. Ruff, B. D. Gaulin, and S. E. Nagler, J. Phys.: Conf. Series **251**, 012058 (2010).
[17] A. Schenck, *Muon Spin Rotation Spectroscopy: Principles and Applications in Solid State Physics* (Bristol: Adam Hilger, 1985).
[18] S. Lee, S. Kilcoyne, and R. Cywinski, Chemistry and Materials, Proceedings of the 50th Scottish University Summer School in Physics **51** (1998).
[19] Y.J.Uemura, Muon Science pp. 85–114 (1999).
[20] O. V. Kovalev, *Irreducible Representations of the Space Groups* (Routledge, 1965).
[21] A. Wills, Physica B: Cond. Matter **276**, 680 (2000).
[22] P. Meier, J. Chappert, and R. Grynszpan, *Muons and pions in materials research* (1984).
[23] H. Maeter, H. Luetkens, Y. G. Pashkevich, A. Kwadrin, R. Khasanov, A. Amato, A. A. Gusev, K. V. Lamonova, D. A. Chervinskii, R. Klingeler, et al., Phys. Rev. B **80**, 094524 (2009).
[24] A. P. Murani, Phys. Rev. B **28**, 2308 (1983).
[25] A. P. Murani, Phys. Rev. B **50**, 9882 (1994).
[26] E. A. Goremychkin and R. Osborn, Phys. Rev. B **47**, 14280 (1993).
[27] V. F. Sears, Neutron News **3**, 26 (1992).
[28] W. Bao, P. G. Pagliuso, J. L. Sarrao, J. D. Thompson, Z. Fisk, J. W. Lynn, and R. W. Erwin, Phys. Rev. B **62**, R14621 (2000).
[29] C. Stock, J. A. Rodriguez-Rivera, K. Schmalzl, E. E. Rodriguez, A. Stunault, and C. Petrovic, Phys. Rev. Lett. **114**, 247005 (2015).
[30] E. Fawcett, Rev. Mod. Phys. **60**, 209 (1988).
[31] Y. Sidis, M. Braden, P. Bourges, B. Hennion, S. NishiZaki, Y. Maeno, and Y. Mori, Phys. Rev. Lett. **83**, 3320 (1999).
[32] I. I. Mazin and D. J. Singh, Phys. Rev. Lett. **82**, 4324 (1999).
[33] G. Lawes, A. B. Harris, T. Kimura, N. Rogado, R. J. Cava, A. Aharony, O. Entin-Wohlman, T. Yildirim, M. Kenzelmann, C. Broholm, et al., Phys. Rev. Lett. **95**, 087205 (2005).
[34] Y. Akagi, M. Udagawa, and Y. Motome, Phys. Rev. Lett. **108**, 096401 (2012).
[35] S. Hayami and Y. Motome, Phys. Rev. B **90**, 060402 (2014).
[36] T. McQueen, T. Klimczuk, A. Williams, Q. Huang, and R. Cava, Physical Review B **79**, 172502 (2009).
[37] J. Rodriguez-Carvajal, in *Satellite meeting on powder diffraction of the XV congress of the IUCr* (Toulouse, France:[sn], 1990), vol. 127.
[38] J. Zhao, Q. Huang, C. de La Cruz, S. Li, J. Lynn, Y. Chen, M. Green, G. Chen, G. Li, Z. Li, et al., Nature Mat. **7**, 953 (2008).
[39] G. Kresse and J. Furthmuller, J. Comp. Materials **6**, 15 (1996).
[40] G. Kresse, Phys. Rev. B **54**, 11169 (1996).

[41] G. Kresse and J. Hafner, Phys. Rev. B **43**, 558 (1993).
[42] C. Kittel, *Introduction to Solid State Physics* (Wiley, 2005).
[43] E. Heltemes and C. Swenson, J. Chem. Phys. **35**, 1264 (1961).
[44] C.D.Bredl, S.Horn, and F. Steglich, Phys. Rev. Lett. **52**, 22 (1984).
[45] K. W. H. Stevens, Proc. Phys. Soc. A **65**, 209 (1952).
[46] S. Lovesy, *Theory of magnetic neutron and photon scattering* (1989).
[47] J. Jensen, J. Magn. Magn. Mater. **29**, 47 (1982).

[48] See Supplementary Material for the following information: the sample synthesis [36], details in the Rietveld refinement [37, 38], details in the DFT calculation [39–41], analysis of Schottky anomaly [42–44] in the low-T specific heat, crystal field analysis and corresponding magnetic susceptibility calculation [45–47].